Exp Astron (2016) 42:271–283
DOI 10.1007/s10686-016-9509-y

ORIGINAL ARTICLE

Solar dynamics imaging system a back-end instrument for the proposed NLST

K.B. Ramesh[1] · N. Vasantharaju[2] · P. Hemanth[1] · K. Reardon[3]

Received: 24 August 2015 / Accepted: 8 August 2016 / Published online: 26 October 2016

Abstract The Solar Dynamics Imaging System (SDIS) will be one of the focal plane instruments operated at the National Large Solar Telescope (NLST). The prime objective of the instrument is to obtain high spatial and temporal resolution images of the region of interest on the Sun in the wavelength range from 390 nm to 900 nm. The SDIS provides filtergrams using broad-band filters while preserving the Strehl ratio provided by the telescope. Furthermore, the SDIS is expected to provide observations that allow image reconstruction to extract wave front information and achieve a homogenous image quality over the entire FOV.

Keywords Solar · Broad band imaging · NLST

1 Introduction

National Large Solar Telescope (NLST) is a 2-m class telescope proposed to be installed in the high mountain ranges of Himalayas at an altitude of about 4300 meters for carrying out high-resolution studies of the solar atmosphere. The proposed site is understood to have extremely low water vapour content and is unaffected by monsoons. A state-of-the-art adaptive optics (AO) system integrated with NLST is expected to provide near diffraction limited imaging over entire wavelength range of

✉ Ramesh, K.B.
kbramesh@iiap.res.in

[1] Indian Institute of Astrophysics, Koramangala, Bengaluru, 560034, India

[2] Bangalore University, Bengaluru, Karnataka, India

[3] NSO, Sacramento peak observatory, Sunspot, NM 88349, USA

interest under favourable seeing conditions. NLST will be equipped with high resolution instruments at the back-end that will provide an opportunity for the solar community to attempt many outstanding problems of solar physics. SDIS is one of the three proposed back-end instruments for NLST. A Fabry-Perot based narrow band imager, and a spectropolarimeter are the other two back-end instruments planned for NLST.

The temperatures, velocities, densities, and magnetic fields can evolve very rapidly in the solar atmosphere. In order to understand their structure and dynamics both high spatial and temporal resolution observations are required. High spatial resolution observations are always limited by atmospheric seeing. In order to overcome this situation imaging at a faster rate with exposure times less than 10 ms are required. This constraint limits the number of photons collected that in turn influences the signal-to-noise estimates of the physical parameters. Large aperture telescopes at prime sites such as NLST augmented with high order AO will minimize the atmospheric seeing effects and provide near diffraction limited images within the limited field of view.

The main aim of the SDIS is to obtain the Sun's images at the highest possible spatial and temporal resolution at a number of specified wavelengths in the range 390 nm to 900 nm. This will be accomplished with an optical design that preserves the Strehl-ratio of the imaging provided by the telescope, and that has a high optical throughput at all considered wavelengths. In addition, the SDIS will provide high-quality imaging through filters with relatively broad passbands to optimize throughput and short exposure times to effectively "freeze" the atmospheric turbulence that allow image reconstruction using speckle interferometric or blind deconvolution methods for improving image quality beyond what is provided by the telescope AO system. Simultaneous images obtained in a "multi-spectral" mode are expected to provide co-temporal information on the small-scale activity at different depths in the solar atmosphere.

2 Science with SDIS

2.1 Morphology and structure of sunspots

It is now known that the sunspots are highly structured formations with convective elements (umbral dots) inside of the umbra [24, 32], and of varying magnetic fields across the umbra [13, 16]. Highly dynamic flows and variations of angles within the penumbra, and "light bridges" which often demarcate fracture lines on which sunspots eventually break up make much more complicated to understand them [17]. As with the magneto convective flows in the photosphere, some of the only clues about sunspot structure have come from MHD numerical simulations [22]. However these also require verification and validation through detailed observations of sunspot structure and dynamics using high spatial and temporal resolutions. The SDIS will provide high resolution, fast cadence movies of penumbral fibril formation, umbral flows, and interactions. It will use several wavelength bands to discriminate between various layers in sunspot umbral and penumbral structure. Simultaneous

broad-band imaging and the polarimetric observations of sunspots would help assess role of magnetoconvection in sunspots (umbral dots), light bridges, and penumbral filaments.

2.2 Dynamics of magnetic elements

The foot-points of the magnetic flux tubes, intergranular bright points (igBPs) are clearly visible in lines formed in the photosphere, such as G-band, CN-band, blue continuum and TiO-band [35]. TiO images provide an enhanced gradient of intensity around igBPs, which is very beneficial for imaging them in contrast to the G-band filter. Moreover, the adaptive optics system and the speckle reconstruction code are more efficient when observing at longer wavelengths [1]. IgBPs show a strong spatial correlation with magnetic flux concentrations and are therefore useful as magnetic proxies, which allow the distribution and dynamics of magnetic features to be studied at a higher spatial resolution than using spectro-polarimetric techniques [4, 25, 26]. The radiative properties of igBPs possibly play an important role in influencing the Earths climate [10, 28]). Moreover, the motions of igBPs can influence the granulation and energy transport process in the lower solar atmosphere (e.g., strong magnetic field can suppress normal convective flows [2]). Therefore, the motions can indicate the properties of MHD waves excited at lower solar atmosphere that may contribute to coronal heating, and generate kinetic and Alfven waves and then release energy [3, 7, 20].

Faculae are thought to be the major source of the excess solar irradiance reaching Earth during periods of maximal sunspot activity [11, 27]. By observing faculae embedded in the granulation at the very high spatial and temporal resolutions one can investigate the detailed contribution to the irradiation that faculae provide. The shape and formation of the flux concentrations will be key in determining how to properly model and account for faculae flux in irradiance studies

2.3 Impulsive energy release in active regions

Studies on flux emergence and cancellation of granular scale size features [31] surrounding the filament like structures of penumbral region of sunspots are crucial in order to understand the formation of active regions. The study of small-scale phenomena in an emerging solar active region is important in the perspective of small-scale magnetic loops interacting with pre-existing large-scale magnetic fields [6].

Observational signatures of energy release at different scales and heights have been identified above emerging flux regions (EFRs). For instance, small-scale brightening and transient emissions in the wings of the chromospheric Hα line, known as Ellerman Bombs or EBs [9] belong to such energy release. Even though Ellerman bombs have been observed in the Hα line within emerging magnetic flux regions since the early 20th century, their origin and the mechanisms that lead to their formation have been strongly debated. Except for the hydrogen Hα line, EBs are also observed in CaII H, K, and infrared 8542Å chromospheric lines [5, 19]. EBs with mean scale sizes of about 0.6 arcsec and life times of about 12 sec [14] are generally explained as due to reconnection processes changing the morphology of the rising

magnetic field lines. Braiding of magnetic field as a result of reconnection has been proposed as a possible mechanism for heating upper layers in the solar atmosphere. Observations of X-ray jets (collimated flows of plasma at temperatures of a few million degrees) suggested that the magnetic reconnection that is associated with a violent release of energy may be responsible for heating the corona. But the physical relationship between the X-ray jets, EBs or microflares (localized impulsive bursts whose total energy is below the level of the standard flares) and cooler Hα surges (jets of gas at a temperature of about 10,000 K) has been unclear. In particular, it has been thought that Hα surges and X-ray jets must arise from independent processes, on the grounds that reconnection would heat any plasma to X-ray-emitting temperatures [34]. Explosive events seem therefore to be triggered by forced magnetic reconnection [12, 18]. The magnetohydrodynamic simulations of the reconnection process, which show that X-ray jets and Hα surges can be ejected simultaneously from micro-flares, suggested that the total energy associated with the micro-flares is much greater than previously thought, and may be significant in heating the corona. Multi-wavelength observations of such small scale elements at a high cadence (better than 1 sec) and at high spatial resolutions (better than 0.6 arcsec) are required to understand the flux emergence, cancellations and reconnection processes.

3 SDIS-Instrumentation

SDIS provides filtergrams of selected regions of the Sun. The SDIS is expected to preserve the NLST image quality across the entire field of view and hence identical optical paths are used in four channels of system. Figure 1 shows schematic optical layout of SDIS. The advantage of this arrangement is that images may be obtained in two or more channels simultaneously, effectively increasing the possible cadence in multi-spectral mode.

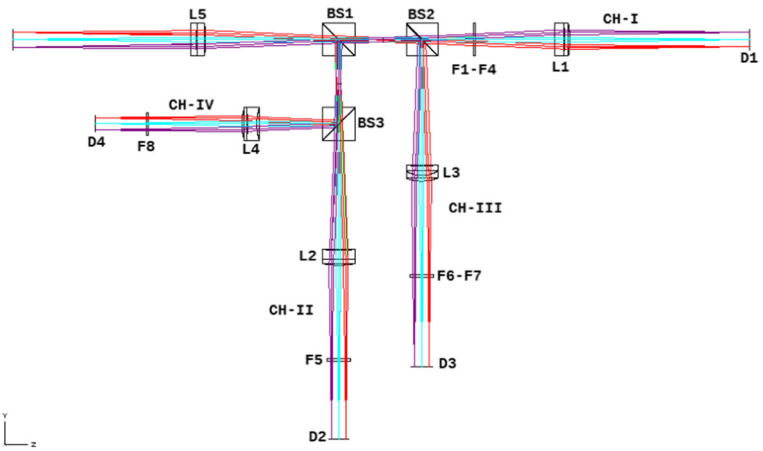

Fig. 1 Schematic of the Solar Dynamics Imaging System. F1-F8: Dielectric filters, L1-L4: Re-imaging lenses, L5: Collimating lens, D1-D4: Detectors, BS1-BS3: Dichroic beam splitters

The wavelengths of interest are divided into four groups (for four channels) according to their wavelengths as dichroic beamsplitters are planned to be used. CN-I (388.3 nm), Ca-II K (393.3 nm), G-Band (430.5 nm) and Blue continuum (432.0 nm) are to be in channel-I, H-beta (486.1 nm) is to be in channel-II, H-alpha (656.3 nm) and TiO (705.8 nm) are to be in channel-III and Ca-II (854.2 nm) is to be in channel-IV. No magnification is assumed for the re-imaging as different detectors with different sizes are to be used. This results in a maximum incident angle of 3.4° for the filters. For broad-band filters such as G-band and blue continuum, this is not significant. However, for sub-Angstrom pass band filters it will be a problem. Thus the re-imaging lenses after collimation are designed in such a way that they produce a nearly telecentric beam and hence the filters are used in telecentric beam instead of collimated beam. This simply broadens the passband (f/40 beam) and the filters of a little narrower passband should be obtained. Assuming an effective refractive index of 1.4 (lower end), if H-beta, H-alpha and Ca-II are to be used in an f/40 telecentric beam, the filters pass bands without broadening (i.e. in parallel beam) should be 0.46Å (0.5Å after broadening), 0.3Å (0.4Å after broadening) and 0.37Å (0.5Å after broadening) respectively.

In the optical design, the distances are maintained roughly as to accommodate the mechanical elements (like Filter wheels, mounts). Spherical doublet is used as collimator, with the constraint of having minimum chromatic focal shifts (as in III channel for 6563Å and 7058 Å). For a given channel, re-imaging lens specifications are fixed. These lenses are also doublets with one aspheric surface (the one with high refractive index is made aspheric). The position of the detectors are fixed but the re-imaging lenses are moved remotely to adjust the focus whenever a filter is changed. Tolerance analysis of the optical components was performed by considering the surface and elemental tolerances. Most of them are precision elements (as the tightest tolerances are for high precision fabrication). Spot diagram for the lowest wavelength is presented which corresponds to one of the worst case performances of the system (Fig. 2).

3.1 Wavelength selection

The wavelengths for the SDIS filters are chosen to provide observations of small scale features from deep down in the photospheric heights through the upper chromosphere. SDIS targets at the dynamics of the small scale features such as magnetic elements, and chromospheric bright points with high spatial and temporal resolutions and is expected to provide better insight into the physics of their fine structures. SDIS provides high resolution filtergrams simultaneously in four wavelengths (See Tables 1 and 2) with suitable passbands targeting the structures of both photosphere as well as chromospheric regions. The source regions and the target features are given in the last two columns of the table.

3.2 Filter pass-bands

As the diffraction limit decreases, the atmospheric dispersion, the variation with wavelength of the atmospheric refraction, called the “spectral differential refraction”,

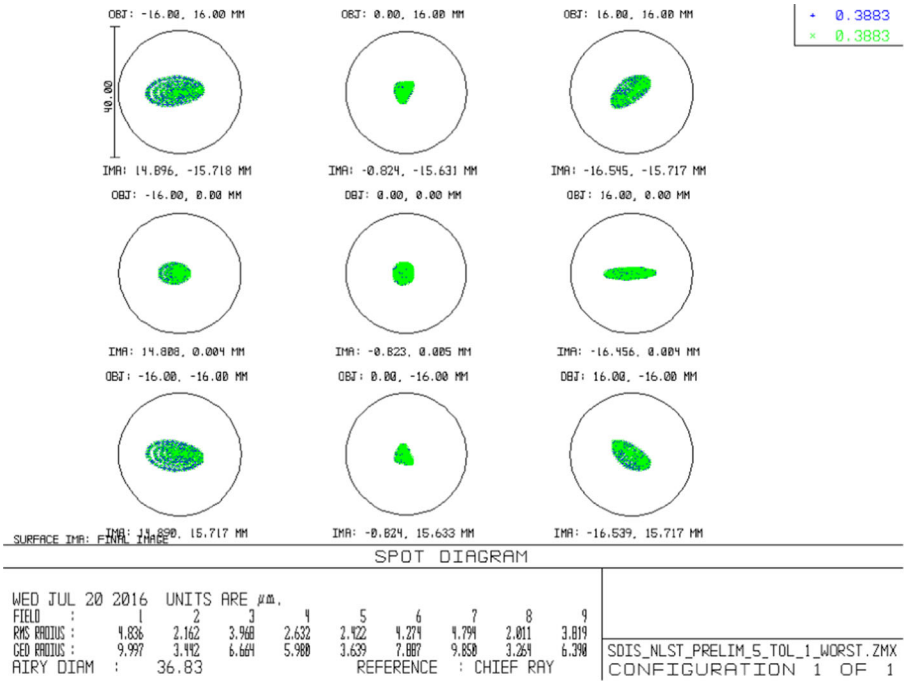

Fig. 2 Spot diagram for one of the worst case performances of the system for λ = 3883 Å

becomes increasingly significant with respect to the resolution element and deserves accurate consideration. The magnitude △R of the spectral differential refraction of a ray at wavelength λ with respect to that at reference wavelength λ_0 is approximately given by,

$$\Delta R = (r_\lambda - r_{\lambda_0})(tanZ_\alpha + \beta tan^3 Z_\alpha) \quad (1)$$

where r_λ is the refractive index of air at wavelength λ, Z_α is the true zenith angle, and β is the ratio of the height of the equivalent homogeneous atmosphere at

Table 1 First set of filters and their details in order to address the dynamics of the small scale features as described in the last column

spectral feature	λ(Å)	Δλ(Å)	Region	Target features
G-band	4305	5	Lower Photosphere	Magnetic element morphology and evolution,granular contrast
Ca II K (line center)	3933	1	Lower chromosphere	Magnetic element morphology, chromospheric dynamics
Tio	7058	6	Photosphere	Sunspot umbral structure and dynamics,granulation contrast
H_β	4861	0.5	Upper chromosphere	Chromospheric dynamics

Table 2 Second set of filters and their details in order to address the dynamics of the small scale features as described in the last column

spectral feature	λ(Å)	Δλ(Å)	Region	Target features
Blue continuum	4320	5	Lower Photosphere	Morphology of active regions
CN I	3883.5	7	Middle Photosphere	Morphology of active regions
Ca II (IR line)	8542	0.5	Upper Photophere /lower chromosphere	Chromospheric morphology and dynamics
H_α	6562.8	0.4	Chromosphere	Penumbral and super penumbral fine structure and chromospheric morphology

the observatory to the geocentric distance of the observatory. The quantity β can be approximated as $\beta = 0.001254T_0/273.15$, where T_0 is the temperature at the observatory in Kelvin.

The effect of spatial smearing on the diffraction limited PSF for the proposed 2-m NLST has been worked out based on the method of [21]. Further the limiting FWHM ($\Delta\lambda$) of the filters that modulates and results in a reduction of the peak transmission of Airy profile by a factor of 0.6, 0.8 and 0.9 have been estimated (Fig. 3). This value for the Strehl ratio implies a possibly tolerable but not altogether negligible degradation in the image quality. Typical filters with a full width of 15Å can result in a notable image degradation at shorter wavelengths. Thus optimum filter pass-band is chosen in between the upper limit of the pass-band as obtained from filter dispersion smeared PSF method [21] and the lower limit of pass-band obtained by careful consideration of factors such as the transmission of nearby spectral lines through the filter is minimized (that is quite evident in Fig. 4 as the Lorentzian filter profiles are over plotted on the solar spectrum), Photon budget, SNR, targeted features and flow velocities.

For each filter the specified filter curve is displayed and compared with the solar atlas spectrum of the corresponding region. Lorentzian profile is assumed for the filter curves. Only two selected Lorentzian filter profiles are shown in Fig. 4.

3.3 Photon budget and SNR considerations

The number of photons that are transmitted by the atmosphere and the optics, and measured by a detector pixel is given by

$$N_\lambda = \frac{\lambda}{hc} I_\lambda t_a t_o T_e \Delta a \Delta\omega \Delta\lambda (QE) \tag{2}$$

where Δa is the area of the solar surface sampled by one pixel and $\Delta\omega$ is the solid angle subtended by the primary mirror as seen from the Sun. h is the Plancks

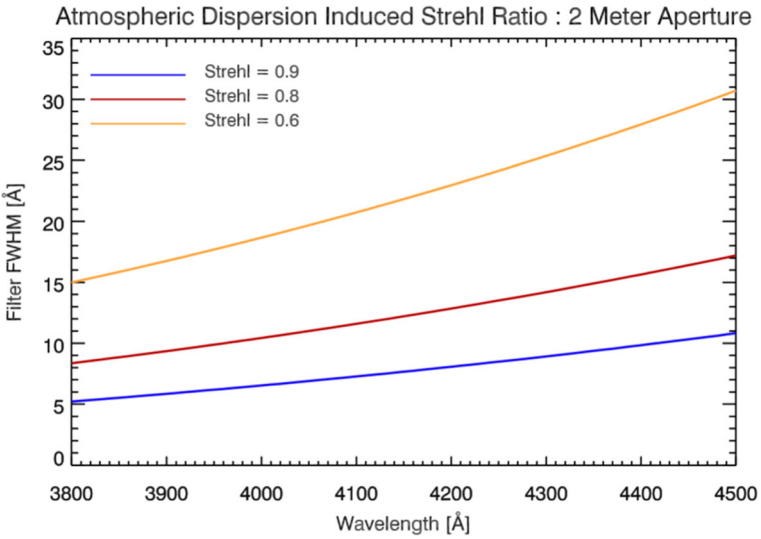

Fig. 3 The FWHM of a simple two cavity filter for which the smearing caused by the relative atmospheric dispersion within the filter passband will reduce the peak intensity of the Airy profile of the telescope of 2 m aperture by a factor of 0.6, 0.8 and 0.9. For example, for G-band ($\triangle\lambda \approx 10$ Å) observations, the strehl ratio will reduces to 0.88, owing to bandwidth smearing

constant, c is the speed of light in vacuum, QE is the quantum efficiency of the detector (QE values for corresponding wavelengths were taken from QE curves in PCO homepage), T_e is the exposure time (for all wavelengths typical exposure time of 10ms is used), $\Delta\lambda$ is the filter passband, t_a and t_o are the transmission of the atmosphere and the instrumentation respectively. The overall optics transmission is taken as 0.42. This factor includes the transmission of the NLST (0.92) as described in the preliminary design of NLST, transmission of 5 elements of SDIS as 98 %, and the combined transmission of three beam-splitters as 0.78. Figure 5 shows the photon flux for all the wavelength bands proposed in the SDIS (left panel). The solar flux intensities (I_λ) at nearby continuum to each considered wavelength are taken from [30].

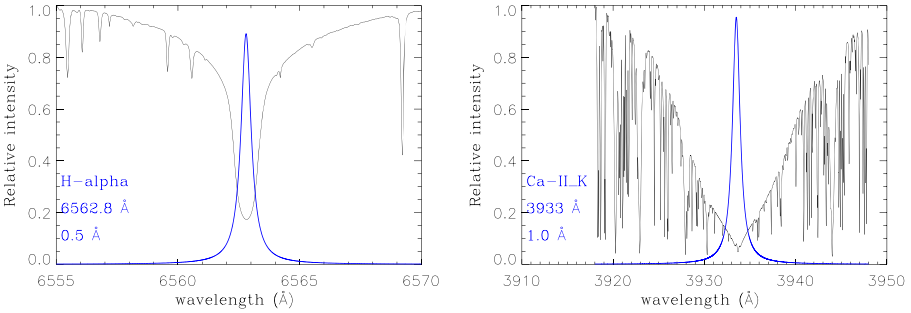

Fig. 4 Solar atlas spectrum and the Lorentzians of the assumed filter profiles

Atmospheric transmission values are taken from [8]. Since the transmission decreases with increasing air mass the photon flux is calculated for four different elevations of the Sun (90°, 45°, 22.5°, 15°). In order to resolve intensity variations of the order of 1 %, a SNR of > 100 is needed. From the current photon budget and SNR considerations (right panel of Fig. 5) it can be seen that this is fulfilled for all wavelength bands.

4 SDIS design specifications

The SDIS will have a total of two filter wheels, one in the I channel and another in the III channel. We optimize the optics specifications such that it works well for two nearby wavelengths of the filters placed in the same filter wheel. It also helps fixing the detectors for each channel.

Each camera in the SDIS will be mounted on a 3-axis linear translation stage. Each stage will have individual control in order to accurately position the detector for correct focus and orientation. Re-imaging lenses positions will be controlled remotely.

4.1 Detector

In order to be able to fully reconstruct the image SDIS is required to have at least two detector pixels spanning the diameter of a resolution element λ/D where D denotes the telescope aperture (in which a perfect telescope concentrates approximately 50 % of the energy of a point source) at each of its specified wavelengths. At this critical sampling, imaging with the shortest wavelength ($\lambda = 3883.5$Å) over full field of view of 200 arc seconds requires a detector of 10K x 10K pixels.

The SDIS requires detector with high quantum efficiencies across the entire visible light spectrum, and sufficiently fast readout device. Readout time for full frame should be less than 0.03 seconds. The large format detectors (10K x 10K) with 10-micron square pixels with fast readout, low noise, high QE are currently unavailable.

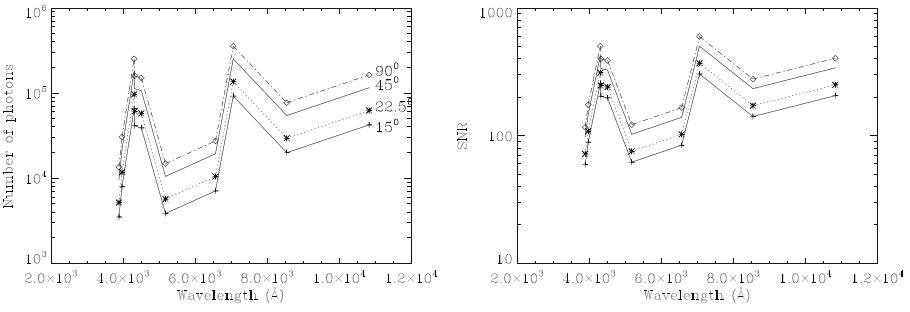

Fig. 5 Estimated photon numbers N_λ (left) and SNR values $\sqrt{N_\lambda}$ (right) for the SDIS wavelengths for four different elevations of the Sun. Exposure time (T_e)= 10 ms

Hence we plan SDIS with the currently available 2k x 2k pixel CCD cameras with 7.5 micron square pixels. Table 3 provides the FOV for each selected wavelength that can be achieved with 2K x 2K format CCD camera at the diffraction limit of NLST (2 pixels per λ/D). We use similar format CCDs for all channels so that the FOV is preserved and the spatial sampling will be adjusted off-line to match simultaneous images from four channels. The mechanical design of the instrument will be required to accommodate larger format cameras when they become available. Each camera will be mounted on a 3-axis precision translation stage.

4.2 Instrument control system

The SDIS will be controlled from a single workstation. The filter wheels, translation stages, and cameras will be controlled using a single user interface. The observer will be able to design sequences of observations by choosing the required filters in the four independent channels. Observations can be planned as single frame mode, multi-frame mode, and burst mode. Also observing (scientific) modes and calibration modes can be defined. Scientific modes could cover time sequences in combinations of wavelength bands that are useful for typical multi-wavelength studies (photospheric mode, chromospheric mode, mixed mode). Calibration mode covers flat fielding, taking dark images and taking grid target images.

SDIS can be operated in a stand-alone mode or in multi-instrument mode. In case of multi-instrument mode different instruments needs to be synchronized and the light beam to be shared in such a way that the photon budget for each instrument is optimized.

In the single frame mode one image is saved per file with user-defined cadence.

In multi-frame mode, a number of images are saved per file with user-defined cadence. This mode will be helpful in maintaining the simultaneity of the SDIS filtergrams and the data obtained from other instruments.

In burst mode large number of images is saved per file to accomplish speckle image reconstruction. However, it requires that nearly 80-100 frames per burst to reconstruct an image. By keeping in view the typical evolution time of solar features, these frames be obtained in a time frame of 2-3 sec. Therefore fast read out cameras (540 Mpixel/s) are required to accomplish the speckle interferometric method.

Table 3 The FOV column refers to the Field Of View achieved with a 2K x 2K pixel detector for each selected wavelength along with their spatial sampling

Wavelength (Å)	spatial sampling (arc second)	FOV (arc second)
3883.5	0.024	49.5
3933	0.0245	50.2
4305	0.027	55.3
4320	0.027	55.3
4861	0.030	61.4
6562.8	0.041	83.9
7058	0.044	90.1
8542	0.0535	109.5

Currently available USB-3.0 supported SCMOS CCDs at a frame rate of 100 per second will be of immense use for speckle observations. With USB 3.0 transfer rate of 5 GBits per sec, nearly 1200 bursts can be obtained in one hour amounting to 1 TB per each channel. Therefore, large temporary storage systems are essential. In this configuration the SDIS will be able to take images at two wavelengths at the same time. In speckle interferometry setup, therefore, two simultaneous science (i.e., reconstructed) sequences are obtained. Although it is out of the scope of this report to bring out details on the image reconstruction methods, we plan to develop the procedures for the alignment, and correction for relative rotation between the different pass-bands required for the reconstruction.

In the frame selection mode only the best images are saved. Selection criteria could be: the rms variation of a cut through the FOV, the rms variation in a user defined sub-region of the FOV, etc. Frame selection mode is expected to slow down the acquisition time.

The ROI mode reads out only the central FOV or a user specified region of the detector. This allows for higher frame rates.

In binned mode the detector performs a user-specified pixel binning. This mode is driven by the requirement to collect enough photons in a short enough period of time to reach an SNR that allows for image reconstruction. The binning mode also allows for faster cadences if image reconstruction is not desired.

4.3 Data calibration

The SDIS filtergrams needed to be corrected for dark current and transmission irregularities caused by dust particles close to focal planes, by inhomogeneities of optical elements and differences of the properties of individual pixels.

4.4 Image reconstruction

The data will be analysed with the help of speckle masking code developed in-house [23, 29]. In this code, a series of short exposure images are processed in the Fourier domain to reconstruct a single high contrast image. Fourier amplitudes are estimated with classical speckle interferometry technique [15] . The Fourier phases are estimated with triple-correlation technique [33]. A sequence of several burst will result in a sequence of reconstructed images and thus it will be possible to study the temporal evolution of small scale features.

5 Summary

SDIS is designed to obtain high resolution images of the Sun simultaneously at four wavelengths to probe the morphology of specific features at different depths in the solar atmosphere. In the light of the very fast dynamics of the chromosphere which is a high science priority for the broad band imaging it is essential to observe as many wavelengths at the same time as possible. SDIS will provide high cadence images to study the time evolution of the solar features such as bright points and magnetic

elements. High speed detectors would allow speckle reconstruction of the features to the near diffraction limit of the telescope.

Acknowledgments The authors thank the anonymous referee for detailed comments and useful suggestions which improved this manuscript. We thank Dr. R. Sridharan for careful reading of this manuscript and providing an insight into the comments (particularly on Filter bandwidth and post-facto image reconstruction). We are also grateful to Prof. K. E. Rangarajan, Dr. B. Ravindra and Dr. K. Sankarasubramanian for helpful discussions that brought significant clarity to the manuscript and to Prof S. S. Hasan for his encouragement and support.

References

1. Abramenko, V., Yurchyshyn, V., Goode, P., Kilcik, A.: Statistical Distribution of Size and Lifetime of Bright Points Observed with the New Solar Telescope. Apjl **725**, L101–L105 (2010)
2. Andić, A., Chae, J., Goode, P.R., Cao, W., Ahn, K., Yurchyshyn, V., Abramenko, V.: Response of Granulation to Small-scale Bright Features in the Quiet Sun. Apj **731**, 29 (2011)
3. Balmaceda, L., Vargas Domínguez, S., Palacios, J., Cabello, I., Domingo, V.: Evidence of small-scale magnetic concentrations dragged by vortex motion of solar photospheric plasma. Aap **513**, L6 (2010)
4. Berger, T.E., Title, A.M.: On the Relation of G-Band Bright Points to the Photospheric Magnetic Field. Apj **553**, 449–469 (2001)
5. Berlicki, A., Heinzel, P.: Observations and NLTE modeling of Ellerman bombs. Aap **567**, A110 (2014)
6. Brooks, D.H., Kurokawa, H., Berger, T.E.: An H α Surge Provoked by Moving Magnetic Features near an Emerging Flux Region. Apj **656**, 1197–1207 (2007)
7. Choudhuri, A.R., Auffret, H., Priest, E.R.: Implications of rapid footpoint motions of photospheric flux tubes for coronal heating. Solphys **143**, 49–68 (1993)
8. Cox, A.N.: Allen's astrophysical quantities, Publisher. AIP Press; Springer, New York (2000)
9. Ellerman, F.: Solar Hydrogen bombs. Apj **46**, 298 (1917)
10. Ermolli, I., Matthes, K., Dudok de Wit, T., Krivova, N.A., Tourpali, K., Weber, M., Unruh, Y.C., Gray, L., Langematz, U., Pilewskie, P., Rozanov, E., Schmutz, W., Shapiro, A., Solanki, S.K., Woods, T.N.: Recent variability of the solar spectral irradiance and its impact on climate modelling. Atmos. Chem. Phys. **13**, 3945–3977 (2013)
11. Fröhlich, C.: Total Solar Irradiance Observations. Surv. Geophys. **33**, 453–473 (2012)
12. Jess, D.B., Mathioudakis, M., Browning, P.K., Crockett, P.J., Keenan, F.P.: Microflare Activity Driven by Forced Magnetic Reconnection. ApjL **712**, L111–L115 (2010)
13. Kopp, G., Rabin, D.: A relation between magnetic field strength and temperature in sunspots. Solphys **141**, 253–265 (1992)
14. Kurokawa, H., Kawaguchi, I., Funakoshi, Y., Nakai, Y.: Morphological and evolutional features of Ellerman bombs. Solphys **79**, 77–84 (1982)
15. Labeyrie, A.: Attainment of Diffraction Limited Resolution in Large Telescopes by Fourier Analysing Speckle Patterns in Star Images. Aap **6**, 85 (1970)
16. Lites, B.W., Thomas, J.H., Bogdan, T.J., Cally, P.S.: Velocity and Magnetic Field Fluctuations in the Photosphere of a Sunspot. Apj **497**, 464–482 (1998)
17. Louis, R.E., Ravindra, B., Mathew, S.K., Bellot Rubio, L.R., Raja Bayanna, A., Venkatakrishnan, P.: Analysis of a Fragmenting Sunspot Using Hinode Observations. Apj **755**, 16 (2012)
18. Nelson, C.J., Shelyag, S., Mathioudakis, M., Doyle, J.G., Madjarska, M.S., Uitenbroek, H., Erdélyi, R.: Ellerman Bombs – Evidence for Magnetic Reconnection in the Lower Solar Atmosphere. Apj **779**, 125 (2013)
19. Pariat, E., Schmieder, B., Berlicki, A., Deng, Y., Mein, N., López Ariste, A., Wang, S.: Spectrophotometric analysis of Ellerman bombs in the Ca II, H α, and UV range. Aap **279-289**, 473 (2007)
20. Parker, E.N.: Nanoflares and the solar X-ray corona. Apj **330**, 474–479 (1988)
21. Reardon, K.P.: The Effects of Atmospheric Dispersion on High-Resolution Solar Spectroscopy. Solphys **239**, 503–517 (2006)

22. Rempel, M.: Numerical Sunspot Models: Robustness of Photospheric Velocity and Magnetic Field Structure. Apj **750**, 62 (2012)
23. Rengaswamy, S., Girard, J., de Wit, W.-J., Boffin, H.: Speckle Imaging with VLT/NACO No-AO Mode. The Messenger **155**, 12–16 (2014)
24. Rimmele, T.: On the Relation between Umbral Dots, Dark-cored Filaments, and Light Bridges. Apj **672**, 684–695 (2008)
25. Schüssler, M., Shelyag, S., Berdyugina, S., Vögler, A., Solanki, S.K.: Why Solar Magnetic Flux Concentrations Are Bright in Molecular Bands. ApjL **597**, L173–L176 (2003)
26. Shelyag, S., Schüssler, M., Solanki, S.K., Berdyugina, S.V., Vögler, A.: G-band spectral synthesis and diagnostics of simulated solar magneto-convection. Aap **427**, 335–343 (2004)
27. Solanki, S.K., Fligge, M.: Reconstruction of Past Solar Irradiance. Ssr **94**, 127–138 (2000)
28. Solanki, S.K., Krivova, N.A., Haigh, J.D.: Solar Irradiance Variability and Climate. Araa **51**, 311–351 (2013)
29. Sridharan, R.: Techniques for Achieving Higher Spatial Resolution. http://hdl.handle.net/2248/123. Ph.D Thesis (2001)
30. Stix, M.: The Sun. an Introduction. Springer-Verlag Berlin Heidelberg, New York (1989)
31. Vargas Domínguez, S., van Driel-Gesztelyi, L., Bellot Rubio, L.R.: Granular-Scale Elementary Flux Emergence Episodes in a Solar Active Region. Solphys **278**, 99–120 (2012)
32. Watanabe, H., Bellot Rubio, L.R., de la Cruz Rodríguez, J., Rouppe van der Voort, L.: Temporal Evolution of Velocity and Magnetic Field in and around Umbral Dots. Apj **757**, 49 (2012)
33. Weigelt, G.P.: Modified astronomical speckle interferometry speckle masking. Opt. Commun. **21**, 55–59 (1977)
34. Yokoyama, T., Shibata, K.: Magnetic reconnection as the origin of X-ray jets and H α surges on the Sun. Nature **375**, 42–44 (1995)
35. Zakharov, V., Gandorfer, A., Solanki, S.K., Löfdahl, M.: A comparative study of the contrast of solar magnetic elements in CN and CH. Aap **437**, L43–L46 (2005)